NANO MICRO small
www.small-journal.com

Directed Vertical Diffusion of Photovoltaic Active Layer Components into Porous ZnO-Based Cathode Buffer Layers

Jia-Jhen Kang, Tsung-Yu Yang, Yi-Kang Lan, Wei-Ru Wu, Chun-Jen Su, Shih-Chang Weng, Norifumi L. Yamada, An-Chung Su, and U-Ser Jeng**

Cathode buffer layers (CBLs) can effectively further the efficiency of polymer solar cells (PSCs), after optimization of the active layer. Hidden between the active layer and cathode of the inverted PSC device configuration is the critical yet often unattended vertical diffusion of the active layer components across CBL. Here, a novel methodology of contrast variation with neutron and anomalous X-ray reflectivity to map the multicomponent depth compositions of inverted PSCs, covering from the active layer surface down to the bottom of the ZnO-based CBL, is developed. Uniquely revealed for a high-performance model PSC are the often overlooked porosity distributions of the ZnO-based CBL and the differential diffusions of the polymer PTB7-Th and fullerene derivative $PC_{71}BM$ of the active layer into the CBL. Interface modification of the ZnO-based CBL with fullerene derivative PCBE—OH for size-selective nanochannels can selectively improve the diffusion of $PC_{71}BM$ more than that of the polymer. The deeper penetration of $PC_{71}BM$ establishes a gradient distribution of fullerene derivatives over the ZnO/PCBE-OH CBL, resulting in markedly improved electron mobility and device efficiency of the inverted PSC. The result suggests a new CBL design concept of progressive matching of the conduction bands.

1. Introduction

Cathode buffer layers (CBLs) play a critical role in bridging the electron transport from the active layer to the cathode of inverted polymer solar cells (PSCs), comprising phase-separated nanodomains of charge donor (usually conjugated polymers) and acceptor (typically fullerene derivatives).[1,2] An effective CBL is nearly indispensable to stretch further the efficiency of a PSC, after optimization of the active layer. With the conduction band edge at −4.14 eV, ZnO is the most often used CBL material to facilitate electron transport from the active layer of fullerene-based PSCs to the indium tin oxide (ITO) cathode in the inverted device configuration.[3,4] In addition, vertical segregation of the active layer components for an enriched fullerene concentration near the ZnO-based CBL would be particularly favorable, because fullerene derivatives such as $PC_{71}BM$ have the lowest unoccupied molecular orbital level (LUMO) of ≈−4.0 eV that matches properly the ZnO conduction band for improved electron transportation to the ITO cathode (with Fermi level of ≈−5.0 eV).[3,4] Ever since the use of CBL in bulk-heterojunction PSCs, various interface engineering techniques have been proposed to improve interfacial contacts and electronic properties.[1–7] For example, CBLs were doped with complementary elements[8,9] or small molecules to fine-tune the CBL energy gap structure for specific fullerene derivatives used.[10] Hidden between the active layer and the cathode of PSCs, the structures of such doped CBLs and the vertical diffusion of the active layer components over the CBLs are left unattended largely. As a result, increasingly higher complexity with multidopants of CBLs leads to increasingly higher ambiguity in the mechanism of the improved device performance.[4] The ambiguity associates deeply with the unknown diffusion behavior of the active layer into the doped CBLs, which could not be accounted for in the theoretical design of the energy bands of the CBLs.[11–13]

Dense packing, high optical transmittance, and large interface area for good contact with the active layer, in addition to matching of electron energy levels, are also key features of an effective CBL for inverted PSCs, in which light illuminates into the active layer through the transparent cathode.[12–15] Lying between the active layer (a few hundreds of nanometers in thickness) and the cathode, nanostructural features of the thin CBL of a few tens of nanometers are difficult to probe. Up to the present, most of the morphological observations of the CBLs used in inverted PSCs were largely observed without coverage

J.-J. Kang, W.-R. Wu, Dr. C.-J. Su, Dr. S.-C. Weng, Prof. U-S. Jeng
National Synchrotron Radiation Research Center
Hsinchu Science Park
Hsinchu 30076, Taiwan
E-mail: usjeng@nsrrc.org.tw
T.-Y. Yang, Prof. A.-C. Su, Prof. U-S. Jeng
Department of Chemical Engineering
National Tsing Hua University
Hsinchu 30013, Taiwan
E-mail: acsu@mx.nthu.edu.tw
Dr. Y.-K. Lan
Materials and Electro-Optic Research Division
National Chung Shan Institute of Science and Technology
Taoyuan 32546, Taiwan
Dr. N. L. Yamada
Institute of Materials Structure Science
High Energy Accelerator Research Organization
Tokai, Naka 319-1106, Japan
The ORCID identification number(s) for the author(s) of this article can be found under https://doi.org/10.1002/smll.201704310.

DOI: 10.1002/smll.201704310

© 2018 WILEY-VCH Verlag GmbH & Co. KGaA, Weinheim

of the active layer, using surface-sensitive imaging tools such as atomic force microscopy (AFM) and scanning electron microscopy.[1–4,16] In a few cases, destructive probing with X-ray photoelectron spectroscopy (XPS) and secondary ion mass spectrometry (SIMS) were employed to reveal the depth-dependent atomic ratios of the CBLs covered with PSC active layers, via depleting the above active layer as a function of film bombardment time.[5,17,18] The thus measured atomic ratios across the unevenly destroyed PSC film with XPS or SIMS, however, provide little nanostructural features of the CBLs.[5,16,19]

In a previous study, we have developed a contrast variation methodology with X-ray and neutron reflectivity (XR and NR) to elucidate the through-thickness composition profiles in a conventional PSC active layer containing poly(3-hexylthiophene) (P3HT) and [6,6]-phenyl C61 butyric acid methyl ester ($PC_{60}BM$),[20] on the basis of the different scattering strengths of the conjugated polymer and fullerene derivative to X-rays and neutrons.[21] Combined analysis of XR/NR reflectivity profiles of the stratified film structure could resolve the depth-dependent distributions of the conjugated polymer and fullerene derivative.[20,22] For multicomponent systems of inverted PSCs with metallic-based CBLs, we propose to extend the previous method by including in anomalous XR, which provides rich contrast variations near the X-ray absorption K-edge of the metallic atoms of the CBL, via tuning synchrotron X-ray energy.[23–25] In addition, complimentary NR is included to provide distinct contrasts to anomalous XR.[26–28] Here, we demonstrate that the proposed contrast variation with neutron and anomalous X-ray reflectivity can map the vertical distributions of the relevant components in a model PSC with ZnO-based CBLs, unprecedentedly from the surface of the active layer, across the interfacial zone, down to the bottom of the ZnO-based CBL. Our result unveils a long overlooked porous structure of the ZnO-based CBLs.[1,2,29] The resolved structural details further elucidate differential penetration behavior of the active layer components into the porous ZnO-based CBL. Moreover, we demonstrate that a C_{60}-doped CBL could effectively change the interface features and form size-selective nanochannels, thereby selectively improve more the diffusion of $PC_{71}BM$ from the active layer into the CBL. The deeper penetration of $PC_{71}BM$ could establish a gradient and continuous fullerene distribution over the ZnO–C_{60} CBL, leading to substantially enhanced electron conduction and hence improved power conversion efficiency (PCE).[3] The unique contrast variation methodology of neutron and anomalous X-ray reflectivity proposed here paves a way to resolve even more complicated interface structures of further advanced PSCs with multidoped ZnO CBLs.

2. Results and Discussion

2.1. Depth Composition Mapping Using Neutron and Anomalous X-Ray Reflectivity

The in-plane averaged density or scattering-length-density profile $\overline{\rho}(z)$ of a stratified film through the film thickness can be reconstructed from an XR or NR profile measured as a function of the scattering vector q_z along the film normal.[21] For a n-component system, $\overline{\rho}(z) = \sum_{(i=1)}^{n} f_i(z)\rho_i$ is contributed by the n components of the corresponding scattering length density ρ_i, weighted by the depth-dependent volume fraction $f_i(z)$. Therefore, resolving the $f_i(z)$ profiles of the n-component system requires n sets of $\overline{\rho}(z)$ profiles reconstructed respectively from n sets of reflectivity profiles measured for the same film structure, with varied scattering contrasts. This can be achieved by anomalous XR measurements for a same film, with X-ray energy, E, tuned near and away the absorption K-edge of the selected metallic atoms of the film for varied $\overline{\rho_{E_i}}(z)$ values. Thus, the depth-dependent composition profiles of the film can be solved by the following relations arranged in a matrix form

$$\begin{bmatrix} \overline{\rho_{E_1}}(z) \\ \overline{\rho_{E_2}}(z) \\ \vdots \\ \overline{\rho_{E_n}}(z) \end{bmatrix} = \begin{bmatrix} \rho_{1,E_1}\ \rho_{2,E_1}\cdots\rho_{n,E_1} \\ \rho_{1,E_2}\ \rho_{2,E_2}\cdots\rho_{n,E_2} \\ \cdots\cdots\cdots \\ \rho_{1,E_n}\ \rho_{2,E_n}\cdots\rho_{n,E_n} \end{bmatrix} \begin{bmatrix} f_1(z) \\ f_2(z) \\ \vdots \\ f_N(z) \end{bmatrix} \quad (1)$$

where $\overline{\rho_{E_i}}(z)$ is individually deduced from the model fitting of corresponding anomalous XR data measured with X-ray energy E_i. For better resolution, one of the relations in the matrix (Equation (1)) can be replaced by that of NR for enhanced contrast variation; because fullerene derivatives often used in PSCs have a much higher neutron scattering-density-density ρ_N than that of the conjugated polymers, thereby, providing a higher scattering contrast for increased sensitivity to fullerene distribution.[26–28]

We apply the above methodology to map the depth composition of a model PSC, comprising the active layer of conjugated polymer PTB7-Th and C_{70}-derivative $PC_{71}BM$ and a ZnO-based CBL selectively doped with a C_{60}-derivative PCBE-OH.[3] Three sets of anomalous XR profiles measured with the three X-ray energies of E_1 = 9400 eV, E_2 = 9651 eV, and E_3 = 9656 eV (near the absorption K-edge E_K of Zn in ZnO), complemented with one set of NR data, are used to solve the depth-dependent distributions of the four components in the system from the surface of the PSC active layer down to the bottom of the CBL. As illustrated in **Figure 1**, the X-ray scattering-length-density $\overline{\rho_x}(E)$ measured for a neat ZnO film (detailed in Figure S1 and Table S1 in the Supporting Information) decreases systematically as E approaches E_K,[30] thereby providing systematic changes in scattering contrasts of ZnO relative to the other components of the model PSC active layer. The corresponding X-ray and neutron scattering length densities of the active layer components and the fullerene derivative embedded in the CBL are summarized in Table S2 in the Supporting Information.

2.2. Fullerene Distribution of the ZnO/PCBE-OH CBL

Shown in **Figure 2** are the XR (measured with E_2) and NR data measured for a ZnO film doped with C_{60}-derevative PCBE-OH (ZnO–C_{60}). With the two sets of XR and NR data, we could resolve the two volume-fraction (or composition) distributions $f(z)$ of ZnO and PCBE-OH in the vertical direction of the film. The limited and fast damped Kiessig fringes in the reflectivity profiles imply a general stratified film structure with broad surface/interfaces transition zones (or roughness). From the frequency of the fringes, the overall film thickness is estimated

© 2018 WILEY-VCH Verlag GmbH & Co. KGaA, Weinheim

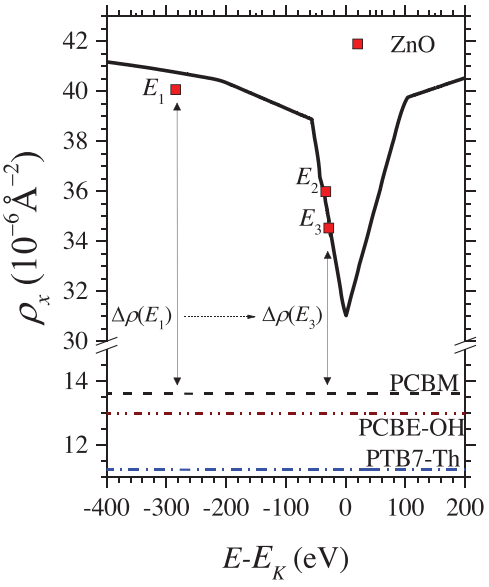

Figure 1. The $\rho_x(E)$ values obtained from the XR data measured for a standard ZnO flake, using the three X-ray energies of E_1 = 9400 eV, E_2 = 9651 eV, and E_3 = 9656 eV. The $\rho_x(E)$ values are overlapped with a calculated profile (solid curve) with E_K for the K-edge absorption of Zn in ZnO. Also shown are the energy-independent ρ_x values of PTB7-Th, $PC_{71}BM$, and PCBE-OH, illustrating the changes of their scattering contrasts $\Delta\rho(E)$ with respective to $\rho_x(E)$ of ZnO.

to be 30 nm. A high film porosity of ≈35% is revealed from the significantly reduced X-ray critical $q_{x,c}$ = 0.033 Å^{-1} for total reflection (reflectivity R = 1.0), compared with that ($q_{x,c}$ = 0.04255 Å^{-1}) for the standard ZnO flake (Figure S1, Supporting Information). Such porosity, overlooked in all previous reports,[1–4] facilitates the permeation of the active layer, as detailed below. We jointly fit the two sets of XR/NR data using a three-layer model (Figure 2b) for $\overline{\rho_x}(z)$ and $\overline{\rho_N}(z)$, with shared fitting parameters in film thickness including a surface layer of 13.5 nm, a major middle homogeneous layer of 10 nm, and a rather compact interfacial layer of 1 nm on top of the Si-wafer substrate. The fitted parameters are summarized in Table S3 in the Supporting Information. The corresponding $f(z)$ profiles of ZnO and the dopant PCBE-OH, deduced using the Equation (1), are shown in Figure 2c. The hence resolve structure of the ZnO–C_{60} film exhibits a constant porosity bottom layer (≈10 nm) of constant ZnO content of f = 55%; above which, the ZnO content diminishes over the broad surface layer (≈15 nm). Correspondingly, the dopant PCBE-OH is found to concentrate mainly in the dense bottom zone (≈10 nm) of the ZnO film, with a saturated doping of ≈10% volume fraction. In the broad surface zone of the ZnO film, PCBE-OH concentration diminishes gradually with the decrease of ZnO content toward film surface. As the total volume fraction should sum up to unity, the result reveals a substantial porosity volume fraction of ≈35% in the dense zone of the ZnO–C_{60} film. The porosity increases exponentially over

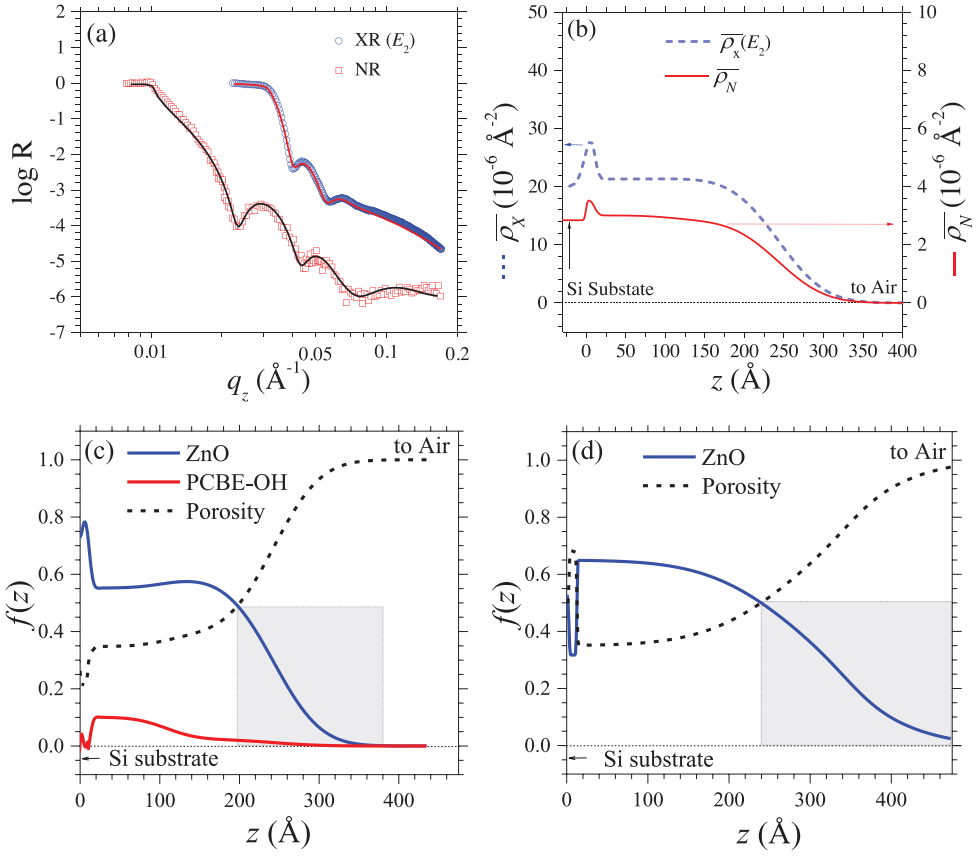

Figure 2. a) XR (measured with E_2) and NR data for the ZnO–C_{60} thin film, fitted (solid curves) using b) the corresponding models of $\overline{\rho_x}$ and $\overline{\rho_N}$ profiles. c) Depth-dependent volume fraction profiles $f(z)$ for the ZnO, porosity, and PCBE-OH components of the ZnO–C_{60} CBL, and d) corresponding $f(z)$ profiles for the ZnO thin film without PCBE-OH doping. Shaded blocks in panels (c) and (d) illustrate the relative sizes of the surface zones.

© 2018 WILEY-VCH Verlag GmbH & Co. KGaA, Weinheim

the porous surface layer, as illustrated in Figure 2c. A parallel analysis for a neat ZnO thin film without dopant PCBE-OH is detailed in Figure S3 and Table S4 in the Supporting Information. The similarly deduced distributions of ZnO and porosity shown in Figure 2d, reveal a more extended and porous surface layer, corresponding to larger surface-segregated ZnO nanodomains as detailed below. Moreover, without PCBE-OH, the interface of the ZnO layer with the Si substrate is of a higher porosity. These structural differences are presumably consequences of changes in surface/interface energies of the ZnO film after intercalation of the fullerene derivative.

2.3. Directed Diffusion of the Active Layer $PC_{71}BM$ into the Porous ZnO–C_{60} Film

The porous feature of the ZnO–C_{60} film revealed above suggests a high possibility of penetration of PSC active layer components into the CBL upon spin coating. Resolving the diffusion (or vertical distribution) of the active layer of PTB7-Th:$PC_{71}BM$ (1:1.5, w/w) into the porous ZnO–C_{60} film requires four sets of XR/NR data. Accordingly, one set of NR data and three sets of anomalous XR data (with E_1, E_2, and E_3) were measured to resolve the vertical distributions of PTB7-Th, $PC_{71}BM$, PCBE-OH, and ZnO of the PSC film. As shown in **Figure 3**a, the XR/NR profiles exhibit prominent and rich Kiessig fringes of a well-stratified film structure. Using the MOTOFIT algorithm,[22] the four sets of XR/NR data could be jointly fitted using a common six-layer model, with shared parameters in sublayer thickness and roughness but independent parameters in scattering-length-density (effect of the contrast variation). The model describes the PTB7-Th/$PC_{71}BM$ active layer (comprising surface, main, and interface layers) sitting on the ZnO–C_{60} CBL (of a similar three-layer structure as that extracted previously) precoated on Si substrate. The combined fitting algorithm places stringent constraints on the fitting model, which needs to concomitantly describe the four sets of XR/NR data (Figure 3a) using the parameters summarized in **Table 1**. The thus fitted $\overline{\rho_x}(E)$ and $\overline{\rho_N}$ profiles (shown representatively in Figure 3b and completely in Figure S4, Supporting Information) illustrate the active layer of ≈85 nm thickness sitting on top of the ZnO–C_{60} CBL (≈30 nm). We notice a nonconformal zone of $\overline{\rho_x}$ and $\overline{\rho_N}$ profiles over the transition (≈10 nm) from the active layer to the ZnO–C_{60} CBL (Figure 3b), suggesting vertical phase segregation of the components across the interface.[20,28] Specifically, the transition zone from the active layer to the CBL exhibits regional increase in $\overline{\rho_N}$ but decrease in $\overline{\rho_x}$, revealing regionally enriched $PC_{71}BM$ because of the distinctly higher $\overline{\rho_N}$ contribution from fullerenes than that from PTB7-Th.[20,28] In contrast, largely conformal $\overline{\rho_x}$ and $\overline{\rho_N}$ profiles in the main active layer zone suggest a vertically uniform composition of PTB7-Th and $PCB_{71}M$.[20,28] Consistently, the correspondingly fitted $\overline{\rho_x}$ and $\overline{\rho_N}$ values (Table 1) are about the same as the mean values ($\overline{\rho_x} = 12.4 \times 10^{-6}$ Å^{-2}) calculated using the prescribed composition of 1:1.5 w/w for PTB7-Th:$PC_{71}BM$. Toward the surface of the PSC film, a much faster decreasing rate of $\overline{\rho_N}$ than that of $\overline{\rho_x}$ indicates a PCBM-depleting (or polymer-enriched) surface zone.[20,28,31]

With the fitted $\overline{\rho_{x,E}}$ and $\overline{\rho_N}$ profiles and the Matrix (Equation (1)), we could deduce all the vertical distributions of the four components from the surface of the active layer down to the bottom of the CBL. As demonstrated in **Figure 4**a, our result clearly elucidates diffusion of the active layer into the porous ZnO–C_{60} buffer layer. Specifically, $PC_{71}BM$ distributes homogeneously in the main PSC layer with $f = 53\%$, which enriches slightly to 57% upon across the CBL. After entering into the CBL, $PC_{71}BM$ diffusion concentration decreases gradually from 10% to 6% over the main ZnO–C_{60}

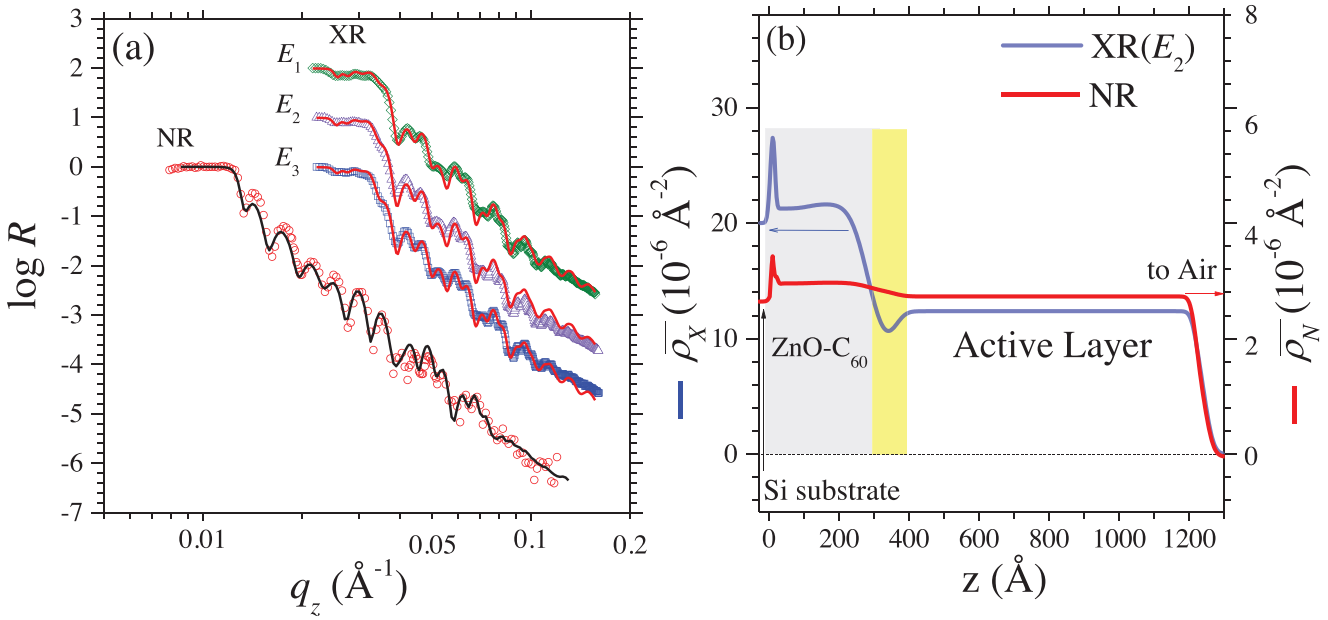

Figure 3. a) NR and anomalous XR data for an active layer of PTB7-Th:$PC_{71}BM$ on a ZnO–C_{60} CBL, spin coated on Si substrate. Data are jointly fitted (solid curves) using b) the $\overline{\rho_x}$ (representatively shown for the E_2 case) and $\overline{\rho_N}$ profiles. For clarity, XR data with E_1 and E_2 are shifted vertically. The shaded zones in panel (b) are the transition zone and the ZnO–C_{60} CBL sitting on Si substrate ($z = 0$).

© 2018 WILEY-VCH Verlag GmbH & Co. KGaA, Weinheim

Table 1. The corefined parameters obtained in the XR/NR joint fitting algorithm on the basis of a common six-layer model for the active layer PTB7-Th:$PC_{71}BM$ (1:1.5, w/w) on a ZnO–C_{60} CBL, spin-coated on Si substrate. The thin SiO_2 layer above the Si substrate, resulted from ozone cleaning of the Si-wafer substrate, is resolved mainly by NR data. Sublayers #1 and #2 are for the active layer, #3 for the transition layer, and #4–#6 for the ZnO–C_{60} CBL. Common fitting parameters are the sublayer thickness t and the interfacial width (roughness) σ.

Sublayer	t [Å]	σ [Å]	$\overline{\rho_x}$ (E_1) [10^{-6} Å^{-2}]	$\overline{\rho_x}$ (E_2) [10^{-6} Å^{-2}]	$\overline{\rho_x}$ (E_3) [10^{-6} Å^{-2}]	$\overline{\rho_N}$ [10^{-6} Å^{-2}]
#1	28 ± 12	17 ± 7	9.4	9.4	9.4	1.7
#2	854 ± 19	13 ± 7	12.4 ± 1.1	12.4 ± 1.0	12.4 ± 1.0	3.0 ± 0.2
#3	76 ± 18	24	8.9	8.8	8.8	3.0 ± 0.4
#4	167 ± 16	40	22.3 ± 1.5	21.6 ± 1.8	20.9 ± 1.8	3.2 ± 0.4
#5	98 ± 17	28	22.3 ± 1.6	21.2 ± 1.1	20.2 ± 1.2	3.1 ± 0.4
#6	11 ± 2	5	33.0 ± 1.6	31.0 ± 1.3	29.1 ± 1.3	3.5 ± 0.7
SiO_2	57 ± 7	7	20.0	20.0	20.0	2.38
Si	Substrate	4	20.0	20.0	20.0	2.05

CBL. We emphasize that the directed $PC_{71}BM$ diffusion can bridge to the distribution of the predoped PCBE-OH of the CBL, thereby, establishing a gradient fullerene distribution throughout the porous ZnO–C_{60} CBL. In contrast, diffusion of PTB7-Th is largely limited to the surface layer of the ZnO–C_{60} CBL, but not to the dense main layer of ZnO–C_{60} (Figure 4a). The selective diffusion behaviors of $PC_{71}BM$ and PTB7-Th to the ZnO–C_{60} CBL result in a favored local phase segregation for enriched $PC_{71}BM$ across the CBL. Moreover, Figure 4a also reveals enriched PTB7-Th at the surface of the active layer, consistent with that revealed qualitatively by SIMS in a previous report.[32] These local vertical phase segregations near the surface and the interfaces are advantageous for the inverted device configuration—with the electron acceptor PCBM enriched throughout the CBL and the electron donor PTB7-Th enriched near the counter active layer interface with the anode.[1,2]

To clarify the PCBE-OH doping effects to the ZnO CBL, parallel XR/NR analysis with a similar PSC active layer on a neat ZnO CBL was also performed (detailed in Figure S5 and Table S6 in the Supporting Information). Illustrated in Figure 4b are the similarly resolved vertical distributions of the relevant components. The result exhibits largely restricted diffusions of the active layer components of $PC_{71}BM$ and PTB7-Th from the denser main ZnO layer. Moreover, unfavorable phase segregation with enriched PTB7-Th in the upper zone of the ZnO CBL occurs. Our theoretical calculations (Table S7, Supporting Information) show that PTB7-Th and ZnO have significantly lower interaction energy of –0.385 kcal Å^{-2}, compared with that of $PB_{71}BM$/ZnO (≈–0.267 kcal Å^{-2}) and $PB_{71}BM$/PTB7-Th (–0.276 kcal Å^{-2}). The higher affinity of PTB7-Th to ZnO surfaces rationalizes the enriched PTB7-Th in the porous surface layer of the ZnO CBL, with rich interfacial areas and large porosity to attract PTB7-Th. In contrast,

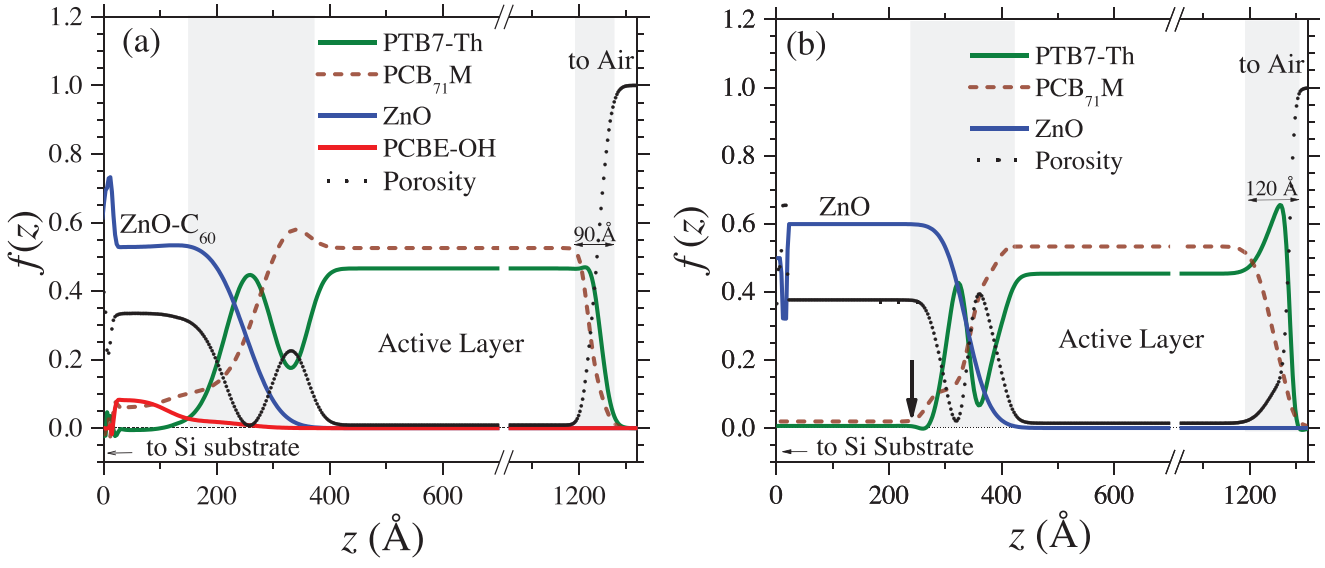

Figure 4. Depth composition (volume fraction) profiles f (z) for the active layers of PTB7-Th:$PC_{71}BM$ (1:1.5, w/w) on a) ZnO–C_{60} and b) ZnO CBLs, respectively. Shaded areas highlight the surface and interface transition zones of distinct phase segregations. The thick arrow in panel (b) marks the termination of the active layer diffusion into the dense bottom zone of the neat ZnO CBL. Note that the homogeneous zone of the active layer is abbreviated.

© 2018 WILEY-VCH Verlag GmbH & Co. KGaA, Weinheim

PCBE-OH decorated ZnO surfaces apparently interact strongly with $PC_{71}BM$ for the selectively improved diffusion throughout the ZnO–C_{60} CBL.

We note that PTB7-Th is enriched in the surface layer of the PSC with either ZnO or $ZnOC_{60}$ CBL (cf. Figure 4a,b), which may be attributed to a lower surface energy E_a = 50.9 mJ m^{-2} of the conjugated polymer, compared with E_a = 53.9 mJ m^{-2} of $PC_{71}BM$ (detailed in Table S8, Supporting Information). The in-depth composition profiles in Figure 4a,b, however, reveal that the ZnO–C_{60} CBL can reduce the active layer surface roughness (transition width) σ to ≈9 from 12 nm of the case with the neat ZnO CBL. Moreover, the surface polymer volume fraction decreases to 47% with the ZnO–C_{60} CBL, compared with the peak value of 65% with the neat ZnO CBL. These changes in surface roughness and surface composition of the active layer are attributed to the more accessible ZnO surfaces of the ZnO–C_{60} CBL, which enhance the polymer diffusion toward the ZnO–C_{60} CBL (due to the high ZnO affinity) for a correspondingly broadened interfacial zone.

A previous report showed that ZnO–C_{60} could provide a negative polaron state 0.39 eV below the LUMO of neat ZnO for a better matching of electron conduction bands of the active layer and ITO cathode.[3] The unveiled structures in Figure 4a elucidate quantitatively that the relatively small amount of PCBE-OH embedded in ZnO–C_{60} CBL can induce significant diffusion of the $PC_{71}BM$ throughout the CBL for a continuous distribution of fullerene derivatives over the CBL. The gradient distribution of the diffused fullerene derivatives and the localized PCBE-OH would provide progressive matching of electron conduction bands over the ZnO–C_{60} CBL, in contrast to the step matching with the neat ZnO CBL of no fullerenes. Consequently observed are the markedly improved electron mobility (μ) to 2.7 × 10^{-3} cm^2 V^{-1} S^{-1} and PCE to 9.4%, compared with μ = 4.9 × 10^{-5} cm^2 V^{-1} S^{-1} and PCE = 7.6% for a similar PSC with a neat ZnO CBL, as that reported previously.[3]

2.4. Interfacial Nanostructure of the ZnO–C_{60} Film

We have further conducted grazing-incidence small- and wide-angle X-ray scattering (GISAXS and GIWAXS) to capture the modified interfacial nanostructures of the ZnO–C_{60} film due to PCBE-OH embedment.[33,34] Shown in **Figure 5**c is the GISAXS pattern measured for the neat ZnO film on Si substrate, exhibiting a prominent rod-like scattering pattern along the out-of-plane scattering vector q_z,[33] with the primary and secondary scattering peaks centered at the in-plane scattering vector q_y = 0.022 and 0.044 nm^{-1}. The result suggests that the porous ZnO film, revealed previously with NR and anomalous XR, comprises a monolayer of surface phase-segregated ZnO nanodomains, packed with a mean spacing of ≈285 nm (estimated from $2\pi/q_y$).[28,35,36] The large domain spacing corresponds to the large surface porosity observed (cf. Figure 4b). The rod-like scattering GISAXS pattern is substantially weakened for the ZnO CBL overlayered with the active layer of PTB7-Th/$PC_{71}BM$ (Figure 5a), which is relevant to the substantial diffusion of PBT7-Th into the highly porous surface layer of the ZnO CBL, hence reduced inhomogeneity in electron density

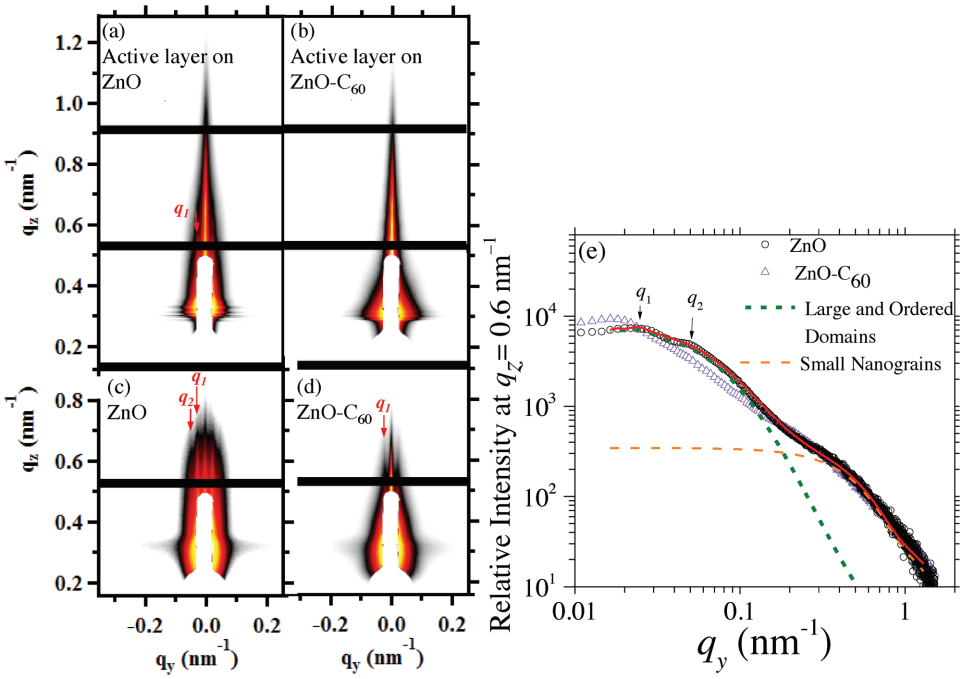

Figure 5. GISAXS 2D patterns of the a) ZnO and b) ZnO–C_{60} films respectively overlayered with the active layer of PTB7-Th:$PC_{71}BM$ (1:1.5 w/w). The arrow marks the observed rod-like scattering peak. Corresponding GISAXS patterns for the c) neat ZnO and d) ZnO–C_{60} films on Si substrate, with the prominent interference peaks indicated by the arrows. e) Representative in-plane GISAXS profiles extracted at q_z = 0.6 nm^{-1} from the corresponding GISAXS patterns, selectively fitted for the ZnO case (solid curve) using a model comprising a monolayer of large and ordered spheroid domains with paracrystalline packing (short-dashed curve) and small prolate nanograins (dashed curve). Note that the overlapped high-q profiles for the two cases are contributed by similar ZnO nanograins.

© 2018 WILEY-VCH Verlag GmbH & Co. KGaA, Weinheim

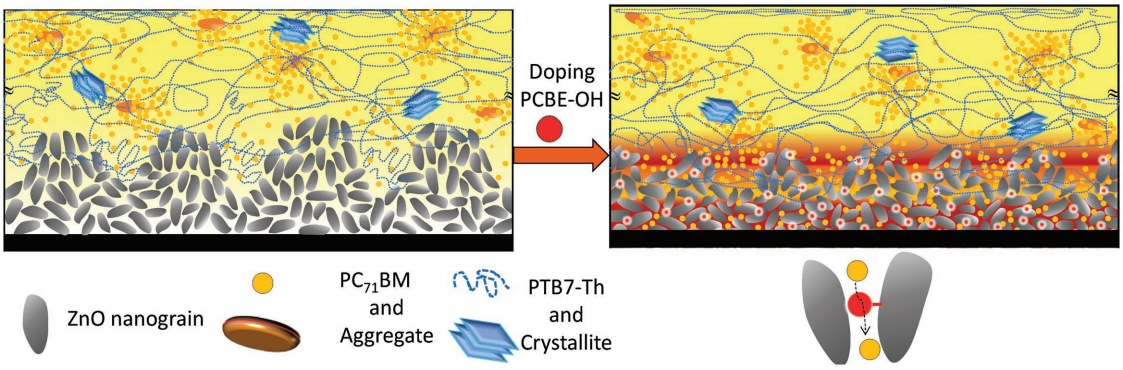

Figure 6. Schematics for the vertical distributions of PTB7-Th and $PC_{71}BM$ of the active layers spin-coated on the ZnO-based CBLs, without (left) or with (right) doping of the fullerene derivative PCBE-OH. Note that the active layer thickness is disproportionally shortened/truncated (marked by ≈) to emphasize structural features of the respective ZnO-based CBL. Selectively tinted (right) are the $PC_{71}BM$ (upper) and PCBE-OH (lower) enriched zones of the ZnO–C_{60} CBL, forming a gradient fullerene distribution over the CBL. The bottom-right cartoon shows the nanochannel opened by intercalation of PCBE-OH between ZnO nanograins for selective $PC_{71}BM$ diffusion. The PTB7-Th crystallites and $PCB_{71}BM$ aggregates are drawn on the basis of the GISAXS/GIWAXS results for the active layer (Figures S8–S10, Supporting Information).[42,43]

(cf. Figure 4b). In contrast, the GISAXS pattern of the ZnO–C_{60} CBL exhibits only weak rod scattering pattern (Figure 5d), suggesting much less surface nanoscale phase segregation. The weak rod scattering pattern of the ZnO–C_{60} CBL is largely eliminated after overlayered with the active layer (Figure 5b). Such a result is consistent with the enhanced diffusion of the active layer into the porous ZnO–C_{60} CBL for reduced density inhomogeneity across the CBL (cf. Figure 3b; Figure S5b, Supporting Information).

Figure 5e shows representative in-plane GISAXS profiles similarly extracted from the corresponding GISAXS patterns of the ZnO–C_{60} and neat ZnO CBLs (Figure 5e). Other than the difference in the low q_y interference peaks mentioned previously, the two GISAXS profiles exhibit similar scattering features in the higher q_y region (>0.2 nm^{-1}), suggesting that both films comprise similar ZnO nanograins, as also revealed by AFM previously.[36–38] The AFM results reported previously[3] for a similarly prepared ZnO film reveal a consistent porous film structure featured with locally ordered short nanoarrays or nanoridges assembled from small ZnO nanograins (cf. Figure S6, Supporting Information).[3,39] On the basis of the image information, the GISAXS profile for the ZnO CBL could be decently fitted (Figure 5e) using a simplified model comprising a monolayer of in-plane, face-on spheroid domains (with a best-fit spheroid lateral diameter of 133 ± 18 nm and a height of 33 ± 5 nm)[40] arranged in a paracrystalline order with a lattice (or mean-spacing) of 283 ± 28 nm; whereas the higher q data are fitted using relatively small prolate ZnO nanograins of major and minor axes of 10.3 ± 0.1 and 3.1 ± 0.1 nm,[28,41] as elucidated in Figure 5e.

2.5. Structural Model

We integrate all the vertical nanostructural features extracted from NR and anomalous XR and in-plane nanostructures from GISAXS into the structural models shown in **Figure 6**. The models depict the porous ZnO-based CBLs with different extents of surface segregated and ordered nanodomains. Interaction of PCBE-OH in-between ZnO nanograins could form size-selective nanochannels in the ZnO–C_{60} CBL (leading to the slightly reduced ZnO volume fraction revealed in Figure 4a), which selectively facilitate the diffusion of $PC_{71}BM$ (of a comparable size to the PCBE-OH intercalated nanochannels) into the CBL from the active layer side. PCBE-OH directed vertical diffusion of $PC_{71}BM$ establishes a continuous and gradient fullerene distribution through the ZnO–C_{60} CBL. Such a gradient fullerene concentration across CBL suggests a new CBL design concept of progressive matching of the conduction bands, via directed vertical diffusion of the active layer fullerene derivatives throughout the porous, fullerene-decorated ZnO CBL. We note that a small amount of PCBE-OH can effectively change the surface properties and suppress surface phase segregation of the ZnO–C_{60} CBL for the substantially reduced surface segregation and enhanced $PC_{71}BM$ diffusion.

3. Conclusion

We have developed a new methodology on the basis of contrast variation with neutron and anomalous X-ray reflectivity, which can map successfully the multicomponent depth compositions of a model PSC with ZnO-based CBLs. The results reveal the differential vertical diffusion behaviors of the PSC components into the ZnO CBL and the critical yet long overlooked porosity distribution of the ZnO CBL. Advantages of doping ZnO CBLs with fullerene derivatives are illustrated with the modified interfacial structures across the ZnO–fullerene CBL and the selectively enhanced vertical diffusion of the fullerene derivatives from the active layer. The hence established depth-concentration gradient of fullerene derivatives in the ZnO–C_{60} CBL is associated with the improved electron mobility and device performance; which correlation suggests a new CBL design concept with progressive matching of conduction bands for inverted PSCs. With synchrotron anomalous XR for rich scattering contrast variations, the developed methodology opens a new channel to resolve increasingly complicated interface structures and depth compositions of PSCs with multidoped, metal-oxide CBLs.[44]

© 2018 WILEY-VCH Verlag GmbH & Co. KGaA, Weinheim

4. Experimental Section

Sample Preparation: ZnO and ZnO–C_{60} thin films were prepared on Si wafers following the procedures detailed previously,[3] including the synthesis of PCBE-OH. For topping with the PSC thin film, the ZnO and ZnO–C_{60} CBL were respectively spin-coated (1000 rpm) with a chlorobenzene/1,8-diiodooctane (DIO) (97:3, v/v) solution of PTB7-Th (Poly[4,8-bis(5-(2-ethylhexyl)thiophen-2-yl)benzo[1,2-b;4,5-b′]dithiophene-2,6-diyl-*alt*-(4-(2-ethylhexyl)-3-fluorothieno[3,4-b]thiophene-)-2-carboxylate-2-6-diyl)]) and $PC_{71}BM$ ([6,6]-Phenyl-C71-butyric acid methyl ester) with 1:1.5 weight ratio.[3] DIO was removed from the spin-coated films in vacuum.[3,28]

XR/NR Measurements: Anomalous X-ray reflectivity measurements were carried out at the beamline 07 of the Taiwan Light Source (TLS) of the National Synchrotron Radiation Research Center (NSRRC), Hsinchu. The X-ray energy was calibrated with a standard sample of ZnO (0.5 mm in thickness) as detailed in Figure S1 in the Supporting Information. X-ray or neutron scattering vector perpendicular to the film surface is defined by $q_z = 4\pi\lambda^{-1}\sin\theta$, with incident angle θ and X-ray or neutron wavelength λ. NR measurements were conducted at BL16 SOFIA neutron reflectometer in J-PARC/MLF, Japan, with the data collected using the time-of-flight mode.[45,46]

GISAXS/GIWAXS Measurements: Simultaneous GISAXS and GIWAXS data were collected at the 23A SWAXS beamline of the TLS of NSRRC, using a 10 keV X-ray beam[47] and an incident angle of 0.16° or 0.2°. With the film surface defined as *x*–*y* plane, and the X-ray incidence plane as *x*–*z* plane, the in-plane scattering vector is defined by q_y, and out-of-plane scattering vector by q_z, as detailed in Figure S7 in the Supporting Information. A Pilatus 1M-F area detector and a CMOS flat panel detector C9728-DK were located at the sample-to-detector distances of 4797 and 150 mm for GISAXS and GIWAXS, respectively.[43]

Supporting Information

Supporting Information is available from the Wiley Online Library or from the author.

Acknowledgements

J.-J.K. and T.-Y.Y. contributed equally to this work. The authors are grateful to Prof. S. A. Chen for introducing this research topic and the generosity support of all samples used. Elaborated sample preparation of H.-J. Jhuo is essential. Assistance of K.-H. Lu in data collection is acknowledged. The neutron experiment at the Materials and Life Science Experimental Facility of the J-PARC was performed under a user program (Proposal No. 2014B0001).

Conflict of Interest

The authors declare no conflict of interest.

Keywords

neutron and anomalous X-ray reflectivity, polymer solar cells, scattering contrast variation, vertical composition profile, ZnO-based cathode buffer layer

Received: December 11, 2017
Revised: January 13, 2018
Published online:

[1] Z. Yin, J. Wei, Q. Zheng, *Adv. Sci.* **2016**, *3*, 1500362.
[2] Z. Liang, Q. Zhang, L. Jiang, G. Cao, *Energy Environ. Sci.* **2015**, *8*, 3442.
[3] S. H. Liao, H. J. Jhuo, Y. S. Cheng, S. A. Chen, *Adv. Mater.* **2013**, *25*, 4766.
[4] S.-H. Liao, H.-J. Jhuo, P.-N. Yeh, Y.-S. Cheng, Y.-L. Li, Y.-H. Lee, S. Sharma, S.-A. Chen, *Sci. Rep.* **2015**, *4*, 6813.
[5] Y. Yan, X. Liu, T. Wang, *Adv. Mater.* **2017**, *29*, 1601674.
[6] S. Nam, J. Seo, S. Woo, W. H. Kim, H. Kim, D. D. C. Bradley, Y. Kim, *Nat. Commun.* **2015**, *6*, 8929.
[7] C.-H. Hsieh, Y.-J. Cheng, P.-J. Li, C.-H. Chen, M. Dubosc, R.-M. Liang, C.-S. Hsu, *J. Am. Chem. Soc.* **2010**, *132*, 4887.
[8] a) L. K. Jagadamma, M. Al-Senani, A. El-Labban, I. Gereige, G. O. N. Ndjawa, J. C. D. Faria, T. Kim, K. Zhao, F. Cruciani, D. H. Anjum, M. A. McLachlan, P. M. Beaujuge, A. Amassian, *Adv. Energy Mater.* **2015**, *5*, 1500204, b) Z. Yin, Q. Zheng, S.-C. Chen, D. Cai, L. Zhou, J. Zhang, *Adv. Energy Mater.* **2014**, *4*, 1301404.
[9] X. Liu, X. Li, Y. Li, C. Song, L. Zhu, W. Zhang, H.-Q. Wang, J. Fang, *Adv. Mater.* **2016**, *28*, 7405.
[10] a) C. Yi, X. Hu, X. Gong, A. Elzatahry, *Mater. Today* **2016**, *19*, 169. b) W. Zhao, L. Ye, S. Zhang, H. Yao, M. Sun, J. Hou, *The J. Phys. Chem. C* **2015**, *119*, 27322.
[11] Z. Liang, Q. Zhang, O. Wiranwetchayan, J. Xi, Z. Yang, K. Park, C. Li, G. Cao, *Adv. Funct. Mater.* **2012**, *22*, 2194.
[12] T. Hu, L.-b. Li, S.-q. Xiao, K. Yuan, H.-j. Yang, L. Chen, Y.-w. Chen, *Org. Electron.* **2016**, *38*, 350.
[13] B. Qi, Z.-G. Zhang, J. Wang, *Sci. Rep.* **2015**, *5*, 7803.
[14] S. Lattante, *Electronics* **2014**, *3*, 132.
[15] L. Znaidi, *Mater. Sci. Eng.: B* **2010**, *174*, 18.
[16] T. Hu, L. Chen, K. Yuan,Y. Chen, *Nanoscale* **2015**, *7*, 9194.
[17] X. Guo, N. Zhou, S. J. Lou, J. Smith, D. B. Tice, J. W. Hennek, R. P. Ortiz, J. T. López Navarrete, S. Li, J. Strzalka, L. X. Chen, R. P. H. Chang, A. Facchetti, T. J. Marks, *Nat. Photonics* **2013**, *7*, 825.
[18] J. Kettle, H. Watersa, Z. Dinga, M. Horie, G. C. Smith, *Sol. Energy Mater. Sol. Cells* **2015**, *141*, 139.
[19] M. A. Ibrahem, H.-Y. Wei, M.-H. Tsai, K.-C. Ho, J. J. Shyue, C. W. Chu, *Sol. Energy Mater. Sol. Cells* **2013**, *108*, 156.
[20] H.-J. Liu, U. Jeng, N. L. Yamada, A.-C. Su, W.-R. Wu, C.-J. Su, S.-J. Lin, K.-H. Wei, M.-Y. Chiu, *Soft Matter* **2011**, *7*, 9276.
[21] R.-J. Roe, *Methods of X-Ray and Neutron Scattering in Polymer Science*, Oxford University Press, Oxford **2000**.
[22] A. Nelson, *J. Appl. Crystallogr.* **2006**, *39*, 273.
[23] J. Als-Nielsen, D. Jacquemain, K. Kjaer, F. Leveiller, M. Lahav, L. Leiserowitz, *Phys. Rep.* **1994**, *246*, 251.
[24] C. Park, P. A. Fenter, *J. Appl. Crystallogr.* **2007**, *40*, 290.
[25] S. Banerjee, Y. J. Parka, D. R. Lee, , Y. H. Jeonga, , K.-B. Lee, S. B. Yoon, H. M. Choi, J.-C. Part, J. S. Roh, M. K. Sanya, *Appl. Surf. Sci.* **1998**, *136*, 41.
[26] J. W. Kingsley, P. P. Marchisio, H. Yi, A. Iraqi, C. J. Kinane, S. Langridge, R. L. Thompson, A. J. Cadby, A. J. Pearson, D. G. Lidzey, R. A. L. Jones, A. J. Parnell, *Sci. Rep.* **2015**, *4*, 5286.
[27] A. J. Parnell, A. D. F. Dunbar, A. J. Pearson, P. A. Staniec, A. J. C. Dennison, H. Hamamatsu, M. W. A. Skoda, D. G. Lidzey, R. A. L. Jones, *Adv. Mater.* **2010**, *22*, 2444.
[28] H.-J. Jhuo, S.-H. Liao, Y.-L. Li, P.-N. Yeh, S.-A. Chen, W.-R. Wu, C.-J. Su, J.-J. Lee, N. L. Yamada, U. Jeng, *Adv. Funct. Mater.* **2016**, *26*, 3094.
[29] R. Lin, M. Miwa, M. Wright, A. Uddin, *Thin Solid Films* **2014**, *566*, 99.
[30] A. Kuzmin, S. Larcheri, F. Rocca, *J. Phys.: Conf. Ser.* **2007**, *93*, 012045.
[31] N. Herath, S. Das, J. Zhu, R. Kumar, J. Chen, K. Xiao, G. Gu, J. F. Browning, B. G. Sumpter, I. N. Ivanov, V. Lauter, *ACS Appl. Mater. Interfaces* **2016**, *8*, 20220.
[32] J. Kong, I.-W. Hwang, K. Lee, *Adv. Mater.* **2014**, *26*, 6275.

© 2018 WILEY-VCH Verlag GmbH & Co. KGaA, Weinheim

[33] G. Renauda, R. Lazzari, F. Leroy, *Surf. Sci. Rep.* **2009**, *64*, 255.
[34] P. Müller-Buschbaum, *Adv. Mater.* **2014**, *26*, 7692.
[35] A. Hexemer, A. P. Müller-Buschbaum, *IUCrJ* **2015**, *2*, 106.
[36] M.-S. Su, C.-Y. Kuo, M.-C. Yuan, U. Jeng, C.-J. Su, K.-H. Wei, *Adv. Mater.* **2011**, *23*, 3315.
[37] D. C. Lim, W. H. Shim, K.-D. Kim, H. O. Seo, J. H. Lim, Y. Jeong, Y. D. Kim, K. H. Lee, *Sol. Energy Mater. Sol. Cells* **2011**, *95*, 2485.
[38] L. K. Jagadamma, M. Abdelsamie, A. El Labban, E. Aresu, O. Guy, N. Ndjawa, D. H. Anjum, D. Cha, P. M. Beaujuge, A. Amassian, *J. Mater. Chem. A* **2014**, *2*, 13321.
[39] N. Sekine, C.-H. Chou, W. L. Kwan, Y. Yang, *Org. Electron.* **2009**, *10*, 1473.
[40] D. Babonneau, *J. Appl. Crystallogr.* **2010**, *43*, 929.
[41] C.-M. Liu, Y.-W. Su, J.-M. Jiang, H.-C. Chen, S.-W. Liu, C.-J. Su, U. Jeng, K.-H. Wei, *J. Mater. Chem. A* **2014**, *2*, 20760.
[42] W.-R. Wu, U. Jeng, C.-J. Su, K.-H. Wei, M.-S. Su, M.-Y. Chiu, C.-Y. Chen, W.-B. Su, C.-H. Su, A.-C. Su, *ACS Nano* **2011**, *5*, 6233.
[43] W.-R. Wu, C.-J. Su, W. T. Chuang, Y.-C. Huang, P.-W. Yang, P.-C. Lin, C.-Y. Chen, T.-Y. Yang, A.-C. Su, K.-H. Wei, C.-M. Liu, U. Jeng, *Adv. Energy Mater.* **2017**, *7*, 1601842.
[44] A. Khassanov, H. G. Steinrück, T. Schmaltz, A. Magerl, M. Halik, *Acc. Chem. Res.* **2015**, *48*, 1901.
[45] N. L. Yamada, N. Torikai, K. Mitamura, H. Sagehashi, S. Sato, H. Seto, T. Sugita, S. Goko, M. Furusaka, T. Oda, M. Hino, T. Fujiwara, H. Takahashi, A. Takahara, *Eur. Phys. J. Plus* **2011**, *126*, 108.
[46] K. Mitamura, N. L. Yamada, H. Sagehashi, N. Torikai, H. Arita, M. Terada, M. Kobayashi, S. Sato, H. Seto, S. Gokou, M. Furusaka, T. Oda, M. Hino, H. Jinnai, A. Takahara, *Polym. J.* **2013**, *45*, 100.
[47] U. Jeng, C. H. Su, C. J. Su, K. F. Liao, W. T. Chuang, Y. H. Lai, J. W. Chang, Y. J. Chen, Y. S. Huang, M. T. Lee, K. L. Yu, J. M. Lin, D. G. Liu, C. F. Chang, C. Y. Liu, C. H. Chang, K. S. Liang, *J. Appl. Crystallogr.* **2010**, *43*, 110.

© 2018 WILEY-VCH Verlag GmbH & Co. KGaA, Weinheim